Journal of Physics and Chemistry of Solids 143 (2020) 109447

Contents lists available at ScienceDirect

Journal of Physics and Chemistry of Solids

journal homepage: http://www.elsevier.com/locate/jpcs

Hydrothermally derived porous carbon and its improved electrochemical performance for supercapacitors using redox additive electrolytes

Palanisamy Rupa Kasturi [a,**], Ramasamy Harivignesh [b], Yun Sung Lee [b], Ramakrishnan Kalai Selvan [a,*]

[a] Energy Storage and Conversion Devices Laboratory, Department of Physics, Bharathiar University, Coimbatore, 641046, Tamil Nadu, India
[b] Faculty of Applied Chemical Engineering, Chonnam National University, Gwangju, 500-757, South Korea

ARTICLE INFO

Keywords:
Artocarpus heterophyllus seed starch
Hydrochar
Activated carbon
Redox additive electrolyte
Supercapacitor

ABSTRACT

The N-rich porous carbon with high surface area is derived from the starch of *Artocarpus heterophyllus seed* (AHS) through hydrothermal carbonization (HTC) followed by KOH chemical activation. The EDLC's are fabricated using nitrogen inherited porous carbon with and without the addition of 0.05 M $VOSO_4$ as redox additive in the pristine 0.5 M H_2SO_4 electrolyte. The device delivered an ultrahigh specific capacitance of 133 Fg^{-1} (at a high current of 15 mA) and high specific energy (32 $Whkg^{-1}$) at a specific power of 936 Wkg^{-1} in the redox electrolyte when compared with pristine 0.5 M H_2SO_4 (92 Fg^{-1}). Similarly, the symmetric redox-mediated EDLC exhibited extended cyclic stability up to 10,000 cycles with a coloumbic efficiency of 97%. These outstanding performance of the fabricated EDLC is due to the excellent faradaic interaction between N-rich, surface-functionalized porous carbon electrode with the redox electrolyte at the electrode-electrolyte interface through the redox reaction between VO^{2+}/VO_2^+ species. The present work corroborates that the combination of hydrothermal derived porous carbon (HPAC) and redox additive electrolyte is a promising way to enhance the specific capacitance of the electric double-layer capacitors.

1. Introduction

Nowadays, porous activated carbon materials are receiving much attention in wide range of exciting applications including electrocatalyst support [1], electrode for energy devices [2] and electrochemical sensors [3], purifier in water remediation [4], etc. due to its extremely high surface area, remarkable porous architecture, and superior electrical conductivity [5,6]. Among the energy storage devices, electric double-layer capacitors (EDLC's) have gained tremendous research interest due to its exceptional energy storage properties. Though EDLC'S has achieved high power density than conventional capacitors [7,8], yet there are few promising factors to achieve high energy density than fuel cell application. Several carbon-based materials including, carbon nanotubes (CNTs) [9], reduced graphene oxide (rGO) [10], carbon foams [11], carbon nanohorns [12], microporous/mesoporous carbon [13], have been utilized as electrodes in EDLC's, owing to their enhanced electrochemical performance. The commercial usage of these materials is limited due to complexity in production and high cost.

Among the carbonaceous materials, porous biomass-derived carbon has several advantages, including, the simple extraction process, abundance, and sustainable [19]. The exceptional heteroatoms inheritance on the biomass-derived carbon surface provides increased wettability, large active sites and exhibits pseudocapacitance during redox reaction in EDLC's. Numerous biomass materials, poplar catkin [14], corn silk [15], watermelon Rind [16], Konjaku Flour [17], charcoal [18], Cucumis melo fruit peel [19], peach gum [20], and waste-metasequoia cone [21], have been used to sequester porous activated carbon materials into outstanding electrodes. Amongst, the agro-waste, *Artocarpus heterophyllus seeds* are not fully exploited and is being exported/disposed to the environs in large amounts (80%) for every year [22]. Statistically, due to over decomposition of a large amount of agro-waste every year into the atmosphere may lead to environmental pollution. Hence, it is essential to convert "*waste into wealth*" by converting biomass into energy. Till now, only a few groups have reported the sequestration of porous activated carbon from *Artocarpus heterophyllus seeds,* considering it as a precursor for the fabrication of electrodes/electrocatalyst support

* Corresponding author.
** Corresponding author.
E-mail addresses: rupaspacy@gmail.com (P.R. Kasturi), selvankram@buc.edu.in (R.K. Selvan).

https://doi.org/10.1016/j.jpcs.2020.109447
Received 23 January 2020; Received in revised form 25 February 2020; Accepted 4 March 2020
Available online 6 March 2020

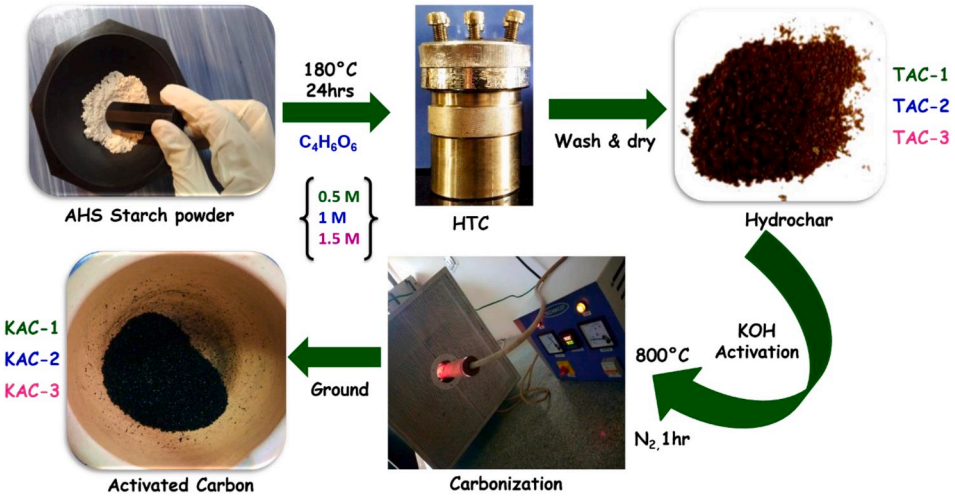

Scheme 1. Hydrothermal derived porous carbon preparation method.

material in energy-based applications [22–24]. Recently, we have reported an all-solid-state EDLC using *Artocarpus heterophyllus seeds* starch derived carbon, which exhibits an energy density of 17 Wh kg^{-1} [22].

It is substantial to improve the specific capacitance of EDLC's to enhance the specific energy, to meet the globalization requirement. Introducing the Faradaic reactions through redox-mediated electrolyte along with the EDLC is the simplest way to accomplish the superior electrochemical EDLC's performance since the electrolytes play a vital role as an interface medium to transport ionic species during the charge-discharge process [25]. So far, *P*-phenylenediamine, *m*-phenylenediamine, hydroquinone (HQ), potassium iodide (KI), indigo carmine, methylene blue, sodium lignosulfonate and vanadyl sulphate ($VOSO_4$), have been widely used as redox additive electrolytes and achieved superior electrochemical performance [26–28]. Amongst, vanadyl sulphate ($VOSO_4$) is an exceptional choice due to its stability, it is an inorganic compound of vanadium and is a source of vanadyl ion, i.e., VO^{2+} (most stable dynamic ion). This inorganic compound is very common in pharmaceutical research; it is easily available, low-cost and easily soluble in an aqueous medium. Inspiringly, Senthil Kumar et al., have described in their report, that VO^{2+}/VO_2^+ is an important ionic species that exhibits a reversible redox reaction at electrode/electrolyte interface and improves their energy storage performance [28].

Considering the preparation strategies, hydrothermal carbonization (HTC) is a prevalent thermochemical conversion technique for the sequestration of carbon-based materials from biomass since it is a very simple, cost-effective and efficient technique. HTC utilizes subcritical water as the solvent medium during the transformation of biomass feedstock into carbonaceous (Hydrochar) product either at higher (300–800 °C) or lower temperature (120–250 °C). The properties of the hydrochar mainly depend upon the four important parameters, including solvent, pH, operation temperature, and residence time. Among these, the pH of the solvent strongly influences the surface chemical characteristics of hydrochar. Even though HTC is a self-induced catalytic reaction; the pH of the reaction tends to vary with respect to residence time, which is adjusted with the addition of acids/alkali based on the requirements. In this regard, different organic acid catalysts such as citric acid, formic acid, acetic acid, sulphuric acid and acrylic acid have been used to decompose bio-macromolecules and induce hydrochar formation. Especially, Tengfei Wang et al., have reported that acetic acid assisted synthesis of hydrochar pellets with pH 2, possess higher heating value, fixed carbon, mass density compared to alkaline NaOH (pH 12). Also, M. ToufiqReza et al., has prepared hydrochar from wheat straw using acetic acid as reaction catalyst and obtained 2.7 times larger surface area than the material obtained at higher pH 12 [29]. Ji Lei Liang et al., have identified that pH (3–7) is suitable for hydrothermal carbonization, whereas, at pH 1, HTC undergoes hydrolysis and speeds up the formation of microsphere at the early stage of the reaction [30]. Based on the analysis, hydrochar formed with low pH (2–4) lead to the formation of microsphere with higher surface area, and solid yield while higher pH results with diffusivity, aggregation and reduces the effective surface area [29–31].

In this line, the present work is concentrated on the preparation of natural sponge-like 3D microporous carbon by hydrothermal carbonization using tartaric acid as the catalyst. Tartaric acid ($C_4H_6O_6$, dicarboxylic acid, TA), which is profoundly present in the citrus fruits, it is an essential crosslinking agent which interacts with two hydroxyls (-OH) and two carboxyls (-COOH) groups, with hydrophilic in nature [32]. So far, TA was utilized as chelating/capping agent during the synthesis of various metal oxide-based compounds through HTC, such as $MnFe_2O_4$ [33], CuO micro-/nanostructures [34], $LiFePO_4$ [35], and ZnO nanostructures [36]. Generally, TA serves as a catalyst that induces HTC mechanism, by increasing the hydroxide ion concentration which results with higher ionic strength and accelerates the reaction rate. Further, it produces hydrochar with tuneable morphology, prevents aggregation, high yield and reduced particle size through hydrolysis (breakdown polysaccharides into smaller fragments). Moreover, the TA catalyst transfer number of carboxyl group to the surface of carbon and enrich the surface functionality of the hydrochar materials [32,35,37]. Previously, we have successfully yielded spherical shaped carbon through citric acid assisted hydrothermal carbonization for electrocatalyst support towards DMFC application. Therefore, to intensify the surface functionality, TA is preferred for the present work to prepare oxygen species-rich high surface area, porous and heteroatom functionalities inherited carbon, which are the essential parameters to enhance the specific energy and thus suits as promising electrodes in EDLCs [7,14].

Hence, with relevance with our previous reports, here, we focused on the preparation of carbon material from *Artocarpus heterophyllus seeds,* with (i) enriched oxygen functionalities and (ii) high surface area and porosity. The desired characteristics of carbon materials were achieved through two-steps, organic catalyst (Tartaric acid) assisted synthesis of hydrothermal carbonization followed by chemical (KOH) activation process. The attained carbon materials were turbostratic in nature, organized with electro-active oxygen functional groups, and inbred with a large number of nitrogen species. Moreover, due to the effect of chemical activation, the morphology of carbon materials was progressed into a natural sea sponge-like 3D microporous carbon with respect to tartaric acid concentration. Such an N-rich sponge-like 3D microporous carbon was employed as electrode material for EDLC's. To further improve the capacitance and faradaic response, the optimized electrodes were sandwiched with redox-mediated H_2SO_4 electrolyte, which

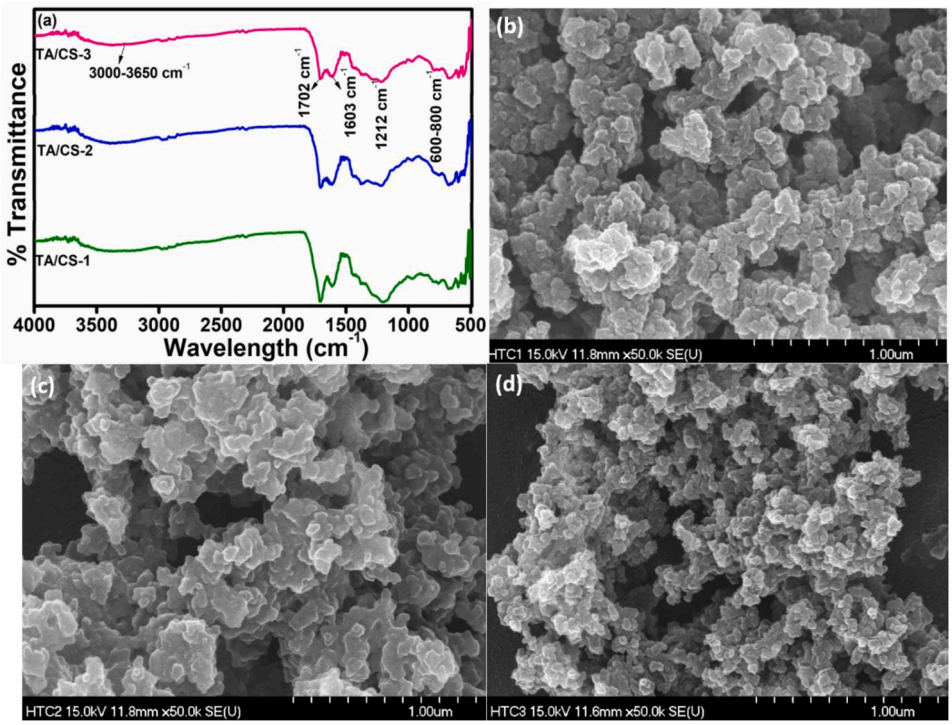

Fig. 1. a) FTIR Spectra and FE-SEM images of b) TAC-1, c) TAC-2 and d) TAC-3.

exhibited a remarkable electrochemical performance with high specific capacitance, extended potential window, superior specific energy and power, and enhanced cycling stability.

2. Experimental methods and materials

2.1. Source and purity of materials

The agro-waste biomass (*Artocarpus heterophyllus seeds*) are collected from the fruit shop, Coimbatore, India. Tartaric acid ($C_4H_6O_6$), Sulphuric acid (H_2SO_4), vanadyl sulphate ($VOSO_4$) are purchased from Merck (India) Ltd., polyvinylidene fluoride or PVDF -$(C_2H_2F_2)$n-with molecular weight of 534,000 are obtained from Sigma–Aldrich (USA), and N-methyl-2-pyrrolidone (NMP) are purchased from Himedia Laboratories Pvt. Ltd. Commercially purchased carbon cloth is treated with concentrated Hydrochloric acid (HCl, Himedia Laboratories Pvt. Ltd) before using it as an electrode substrate. Double distilled water (D-D) is used as the solvent for both experiment and washing reagent throughout the work.

2.2. Preparation of sponge-like 3D mesoporous carbon by KOH activation

The AHS starch solution (5 g/20 ml) is allowed to disperse well in bath sonication for an hour, at room temperature. Simultaneously, different concentrations (0.5, 1, and 1.5 M) of tartaric acid is prepared in 20 mL of D-D water. Subsequently, the prepared tartaric acid solution is added drop by drop into the starch solution and allowed to mix it for 4 h. The obtained sticky colloidal solution (40 ml) is transferred into Teflon lined autoclave with 50 ml capacity and hydrothermally treated at 180 °C for 12 h (Scheme 1). The obtained brown hydrochar is washed thoroughly with D-D water to remove the impurities. Finally, the obtained hydrochar is dried at 80 °C for 12 h and kept in an airtight container. Initially, the desired amount of (2.5 g) of the prepared above hydrochar is soaked with KOH solution (2.5 g/10 ml D-D water) for 24 h under stirring. Subsequently, the activation process is carried out at 800 °C for 1 h under N_2 atmosphere. Finally, the obtained product was washed thoroughly with D-D water and ethanol several times.. Hereafter, the obtained carbon samples are called as KAC-1, KAC-2 and KAC-3, together known as KAC materials.

2.3. Material characterization techniques

The powder X-ray diffraction (PXRD, Rigaku, Cu Kα, wavelength 1.5406 Å) is used to determine the phase purity of the KAC samples. The functional group organization and degree of graphitization for KAC samples are obtained using FTIR (vertex 70, Bruker) and Raman Spectra (LabRAM HR800) in the range of 4000–400 cm^{-1}. The elemental composition present on the surface of KAC samples is determined using XPS analysis (Multifunctional imaging electron spectrometer, Thermo ESCALAB 250 XI). The SEM (Hitachi, S-4800) and TEM (JEOL, JEM-2010) analysis are performed to understand the surface morphology of the KAC samples.

2.4. Electrode fabrication and electrochemical measurements

The working electrode is prepared by mixing the active material (KAC samples) with carbon black and polyvinylidene di-fluoride (PVDF) in the ratio of 80:10:10 containing 0.3 mL of N-Methyl-2-pyrrolidone (NMP). The black precipitate was transferred to 0.5 ml Flat Tube with Cap and sonicated for 20 min. Then, the solution was brush coated on carbon cloth (1.5 × 1.5 cm^2) and allowed to dry for 24 h at 90 °C under a vacuum atmosphere. The electrochemical measurements are performed using cyclic voltammetry (CV) and galvanostatic charge-discharge (GCD) measurements in a three-electrode system, where the KAC samples coated carbon cloth is used as the working electrode, Pt wire and standard Ag/AgCl serves as counter and a reference electrode, respectively. The charge transfer resistance, solution resistance and relaxation time of the system are estimated using electrochemical impedance spectroscopy (EIS) in 100 kHz −0.1 Hz range. Herein, aqueous 0.5 M H_2SO_4 is used as the electrolyte solution to access the electrochemical measurements in the potential range of interest (0–0.8V vs. Ag/AgCl). Specific capacitance (C_{SP}) from CV is calculated using the following equation [25],

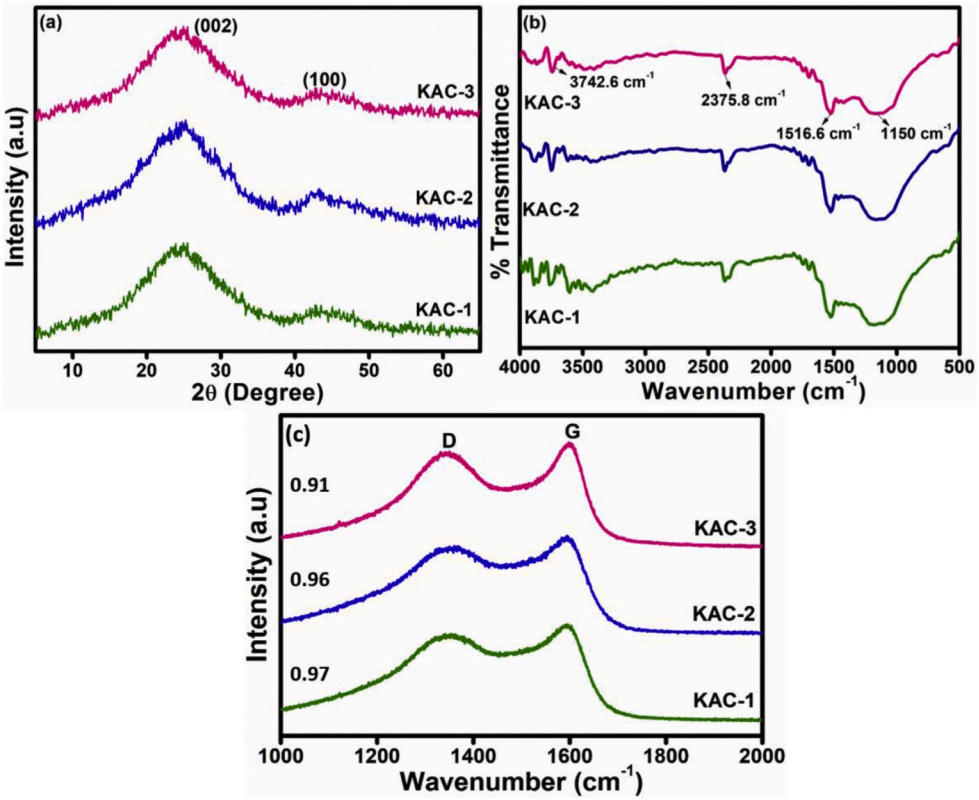

Fig. 2. a) XRD pattern, b) FTIR spectra and C) Raman spectra of KAC materials.

$$C_{sp} = \frac{Q}{(\Delta V \times S \times m)} Fg^{-1} \quad (1)$$

where, Q (C) is the integral area of current and potential charge obtained from CV, m (mg) is the mass loading of the active material (KAC samples) on carbon cloth (i.e. 1 mg/cm^2) and ΔV (V) is the difference in potential range and S (mVs^{-1}) is the scan rate during potential sweep. While the C_{SP} (Fg^{-1}) from GCD is measured by,

$$C_{sp} = \frac{I \times \Delta T}{m \times \Delta V} Fg^{-1} \quad (2)$$

Where, I (mA) is the current, ΔT (s) is the discharge time and m (mg) is the mass loading of active material on carbon cloth.

Further, the symmetric supercapacitor is fabricated using conventional sandwiching method containing, two identical carbon cloth electrodes coated with KAC samples separated by polypropylene separator (1 × 1 cm^2) dipped in a solution containing 0.5 M H_2SO_4 containing various concentrations of $VOSO_4$ (0.01, 0.02, 0.03, 0.04 and 0.05 M). The device fabrication is accomplished in room temperature. The specific capacitance (C_{SP}), specific energy (S_E) and specific power (S_P) are calculated using standard equations.

$$C_{sp} = \frac{I \times \Delta T}{m \times \Delta V} \left(Fg^{-1}\right) \quad (3)$$

$$S_E = \frac{C_{sp} \times \Delta V^2}{2} \left(\frac{Wh}{kg}\right) \quad (4)$$

$$S_p = \frac{S_E \times 3600}{\Delta T} \left(\frac{W}{kg}\right) \quad (5)$$

3. Results and discussion

3.1. Chemical and morphology analysis of hydrochar materials

Fig. 1a shows the FTIR spectra of hydrochar materials prepared with different concentrations of tartaric acid. The obtained spectra exhibit broadband at 3000-3650 cm^{-1}, reveals the domination of hydroxyl group organized on the surface of hydrochar materials due to polysaccharide molecules of AHS. On the other hand, bands at 1702, 1603, 1212, and 600-800 cm^{-1}, inferring the excess presence of carboxyl and carbonyl-containing oxygen functional groups, the footprint of the hydroxyl group, respectively. The results reveal that the TA catalyst promotes hydrothermal carbonization at low temperature and reduces the energy action of AHS starch biomass hydrolysis process [1,2]. The carbonyl-containing oxygen functionalities on the hydrochar surface provide surplus active sites for the occurrence of redox reaction during the electrochemical performance [7].

Fig. 1b-d shows the FE-SEM images of the prepared hydrochar by hydrothermal method using different concentration of tartaric acid. It infers that the hydrochar materials exhibit a patchy morphology with a low concentration of TA (0.5 M). Subsequently, the patchy network gets disintegrated into granules with the increase in tartaric acid concentration (1 M). It is a fact that during hydrothermal carbonization TA induces dehydration reaction and decreases the hydrochar aggregation further. As a result, a granule like morphology is obtained with an increase in TA (Fig. 1c). As, in our previous report [24], AHS starch powder underwent citric acid assisted hydrothermal carbonization at the same condition, which exhibited a sphere-shaped morphology. Therefore, tartaric acid has played a major role in tuning hydrochar with granule shaped morphology organized with surplus organic oxygen functional groups and nitrogen atoms.

Table 1
Calculated parameters from XRD and Raman Analysis.

Sample name	d_{002}	Fa (nm)	L_a (XRD) (nm)	L_c (nm)	N	n	ρ	La (Raman) (nm)
KAC-1	0.354	0.65	2.5	2.0	5	11	2.15	4.0
KAC-2	0.351	0.68	2.7	2.2	6	12	2.17	4.1
KAC-3	0.335	0.70	2.9	2.5	7	14	2.21	4.2

3.2. Physical and chemical characterization of spongy porous activated carbon

XRD pattern of KAC materials (Fig. 2a) exhibits a broad peak observed between 20° and 30°, corresponds to (002) plane, infers the turbostratic structure of activated carbon. The other broad peak between 40° and 50° is attributed to (100) plane, infers the presence of sp^2 hybridized carbon with amorphous nature. The lattice parameters, the thickness and width of the graphitic planes, L_a and L_c, are calculated (Equations (6) and (7)) and are given in Table 1. The interplanar distance (d_{002}) calculated from (002), are similar (>0.3) for all the KAC-materials, and infers the graphitic nature.

$$L_a = \frac{1.84\lambda}{\beta_{100} Cos\theta_{100}} \tag{6}$$

$$L_c = \frac{0.89\lambda}{\beta_{002} Cos\theta_{002}} \tag{7}$$

Where, λ is the X-Ray wavelength (1.54 Å), β (100) and β (002) is the full-width half-maximum of (100) and (002) plane, and θ (100) and θ (002) is the plane of reflection corresponding to (100) and (002) plane. The amorphous degree (Fa) of the obtained materials are calculated using the formula,

$$Fa = \frac{A_{002}}{A_{002} + A_{100}} \tag{8}$$

Where A_{002} and A_{100} are the integrated areas under the (002) and (100) peaks.

Also, N number of layers corresponding to (100) plane, the average number of carbon atoms in an atomic plane (n) and the packing density (ρ) of layers are calculated using,

$$N = \frac{L_C + d_{100}}{d_{100}} \tag{9}$$

$$n = 0.32\, N^2 \tag{10}$$

$$\rho = \frac{0.762}{d_{100}} \tag{11}$$

The overall amorphous degree (F*a*) of KAC materials are found to be 0.65 to 0.71. Also, the decrease in the interplanar distance (d_{002}) infers the development of stacking structure periodicity towards the graphitic structure. Moreover, the thickness of the stacking structure along the c-axis represented as L_c increases with the amorphous degree which interprets the maturity of graphitic structure got increased. With respect to L_c, the number of layers (N) and the number of carbon atoms (n) calculated for KAC materials are 5–7 and 11 to 14, respectively (Table 1). Therefore, the parameters Fa, N, n and ρ value increases with increase in L_c value, infers the evolution of graphitic nature of carbon materials with the increase in TA concentration [38].

FTIR spectra (Fig. 2b), exhibits four strong bands at 3742.6, 2375.8, 1516.6, and 1150 cm^{-1}, inferring the presence O–H group, moisture content present on the surface, C–H stretching due to carboxylic group, C–C stretching to the oxygen bonded to aromatic ether group, and -C-O group, hydroxyl or ether group, respectively. The evolution of activated carbon from hydrochar has lost the broadness of absorption band at 3000-3650 cm^{-1}, region, which infers the exhaustion of O–H groups from the hydrochar due to high-temperature carbonization. Besides, KAC-materials possess a large amount of polar oxygenated functionalities on the surface, holding a mixture of carboxyl and carbonyl functional moieties according to Nikolaos Papaioannou and group [39]. Which infers, due to the strong effect of TA, the organic oxygen functional groups anchored on the surface of hydrochar retains even after carbonization at higher temperature with a slight shift.

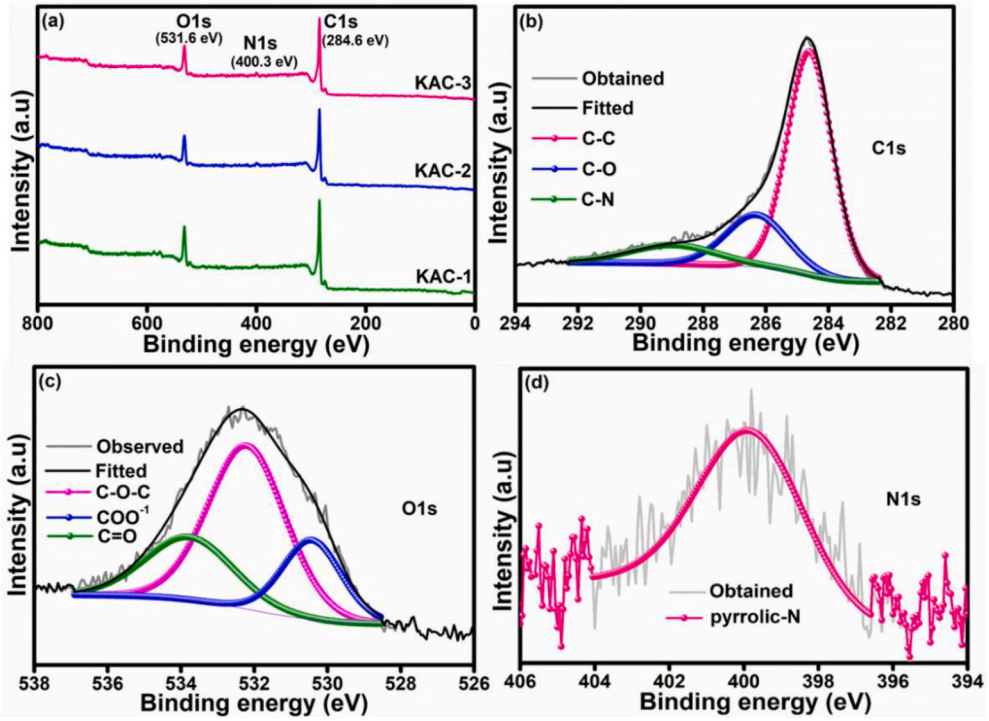

Fig. 3. XPS a) Survey spectra, high-resolution b) C1s, c) O1s and d) N1s of KAC-3.

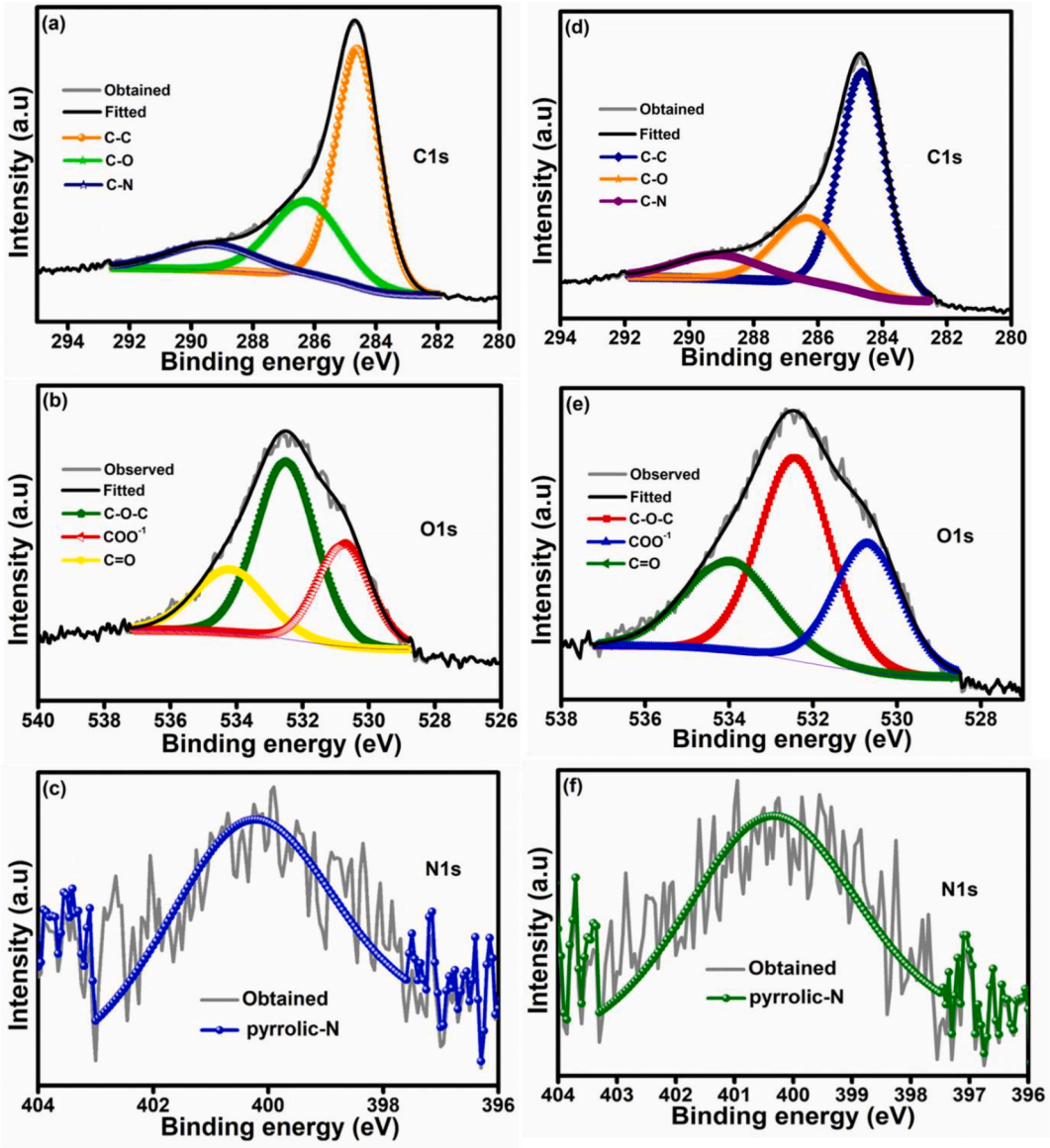

Fig. 4. XPS deconvoluted spectrum of a and d) C1s, b and e) O1s and c and f) N1s of KAC-1 and KAC-2, respectively.

Table 2
Calculated parameters from XPS.

Sample	C1s	Peak B.E (eV)	O1s	Peak B.E (eV)	N1s	Peak B.E (eV)
KAC-1	83.65	284.6	15.59	531.89	0.76	400.26
KAC-2	83.87	284.6	14.31	531.9	1.81	400.20
KAC-3	84.1	284.6	13.69	531.89	2.21	400.01

The Raman spectra (Fig. 2c), of KAC materials, reveals two strong peaks at 1344 cm^{-1} and 1600 cm^{-1}, corresponding to defect (D-peak) and graphitic (G-peak), reveals the disordered graphitic nature and sp^2 hybridization, respectively. The intensity ratio (I_D/I_G) decreases in the order of KAC-3 (0.91) < KAC-2 (0.96) < KAC-1 (0.97) with increasing TA catalyst percentage, reveals the high degree of graphitic of KAC-3 material. Moreover, the *La*, estimated from Raman spectra is less for KAC-3 compared to KAC-1 and KAC-2 material (Table 1), which is in concord with XRD pattern. It is suggested by Wenhua Yu et al., that KOH activation at high temperature corrodes the graphitic structure of carbon material, resulting in a highly disordered porous structure [40]. Herein, the attained values of I_D/I_G and L_a from Raman spectra (Fig. 2c) of KAC-3 purely supports the KOH activation of TA assisted hydrochar with high graphitic ordering by utilizing equal concentration ratio KOH for all the hydrochar materials.

Figs. 3 and 4 shows the XPS analysis of KAC-materials, which is performed to identify and investigate the elemental compositions. The XPS survey spectra (Fig. 3a), reveals the presence of oxygen and nitrogen species other than carbon atoms in the KAC-materials with their corresponding atomic weight percentage (at. Wt. %) are provided in Table 2. The C1s spectrum (Fig. 3b) of KAC-3 is de-convoluted into three peaks at 284.5, 286.4 and 285.4 eV belongs to C1s spectra infer the presence of C–C/C═C group due to graphitic nature, C–O and C–N, respectively. Besides, the O1s spectrum (Fig. 3c) of KAC-3 contains four deconvoluted peaks, 533.7, 532.2, and 530.7 eV attributed to the C–*O*–C group, carboxylic –COO^{-1}, carbonyl (–C═O), respectively. In recent, Zhu et al., have reported in recent that abundant oxygen-containing functional groups are beneficial for improvising the capacitance due to its significant pseudo-capacitance contribution and improved wettability [41].

Further, the nitrogen content in KAC-3 is relatively high compared to KAC-2 and KAC-1 (Table 2), and the N1s spectrum of KAC-3 (Fig. 3d) at 400 eV is deconvoluted into a single peak, belongs to pyrrolic type

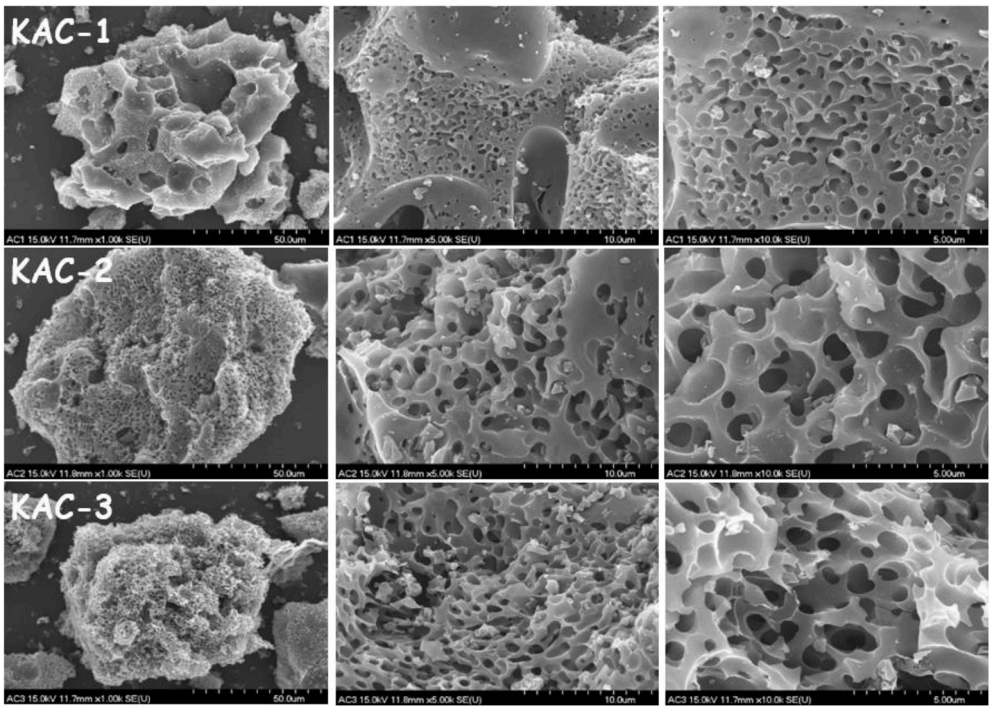

Fig. 5. FE-SEM images of KAC-1, KAC-2 and KAC-3 materials with different magnification.

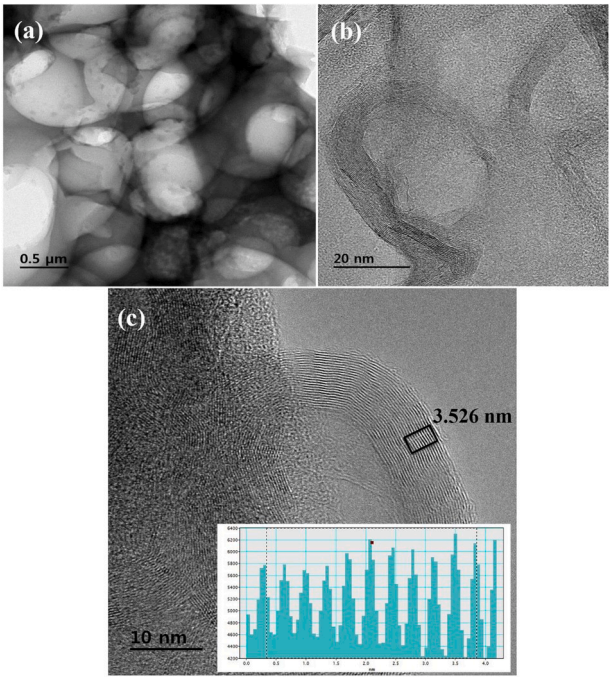

Fig. 6. a) TEM, b) & c) HR-TEM images of KAC-3 material.

nitrogen. According to Han et al., pyrrolic type N is mostly influenced by the carbonization temperature due to the differences in the thermal stability, which is located at the edge sites, bonded to two carbon atoms and is a part of a five-membered ring [42]. Therefore, the combined effect of nitrogen and oxygen functionalities on the carbon surface is anticipated to contribute more defect and large active sites for the accumulation of charge storage during redox reactions. Similarly, the deconvoluted high-resolution spectra of C1s, O1s and N1s of KAC-1 and KAC-2 are shown in Fig. 4(a–d), Fig. 4(b–e) and Fig. 4(c–f), respectively. Therefore, the presence of excess carboxyl and carbonyl functionalities on the surface of carbon materials improves the faradaic capacitance and stability of the devices.

Fig. 5 shows the FE-SEM images of KAC-materials to understand the morphological advancement after high-temperature carbonization. From the observation, the micropores observed on the surface of KAC-materials numerous in the order of KAC-3 > KAC-2> KAC-1. With the increase in TA concentration, KOH activation severely corroded the surface of carbon material, giving rise to uniform natural sea-sponge like "3D mesoporous opening" with undefined edges. In recent, Dina Ibrahim Abouelamaiem et al., have derived carbon through KOH activation from raw pulp material (native cellulose). The obtained carbon exhibited a similar type of spongy shaped morphology with large surface area and porosity [43]. Also, the activated carbon derived from Hemp through hydrothermal carbonization followed by KOH activation delivered a 3D porous carbon structure with large surface area and porosity [44]. Nannan Guo et al., have attained a 3D hierarchical porous structure from lignin as a result of hydrothermal carbonization and KOH activation with enormous surface area and abundant porosity [45].

In reference to the above reports, these 3D spongy mesoporous opening is expected to possess large surface area and porosity, thus provides an opportunity for ions to facilitate to and fro during redox reactions involved in EDLC. Moreover, TEM and HRTEM images shown in Fig. 6 is executed to confirm the surface morphology of KAC-3 material further. TEM image shown in Fig. 6a exhibits thick ring-shaped micropores carbon with 3D linkages, which serves as a reservoir for the ions to traverse freely with low resistance during the EDLC mechanism. Whereas, the HRTEM images (Fig. 6(b and c)), once again reveals the turbostratic nature of carbon material with an interlayer spacing (d_{002}) of 0.36 nm, which is in concord with XRD pattern (Fig. 1a) which is induced from the in-plane diffraction of the material. These values are well-matched with the XRD results.

Fig. 7 shows the representative N_2 adsorption/desorption isotherms and Barrett-Joyner-Halenda (BJH) pore size distributions of KAC-3 material. From the analysis, at low relative pressure (<0.05), the isotherms display strong adsorption, while in the midrange (0.2–0.6), a hysteresis loop is visible and at the high pressure (0.95–1), an upward elevation is clearly visible. Therefore, the existence of hysteresis loop

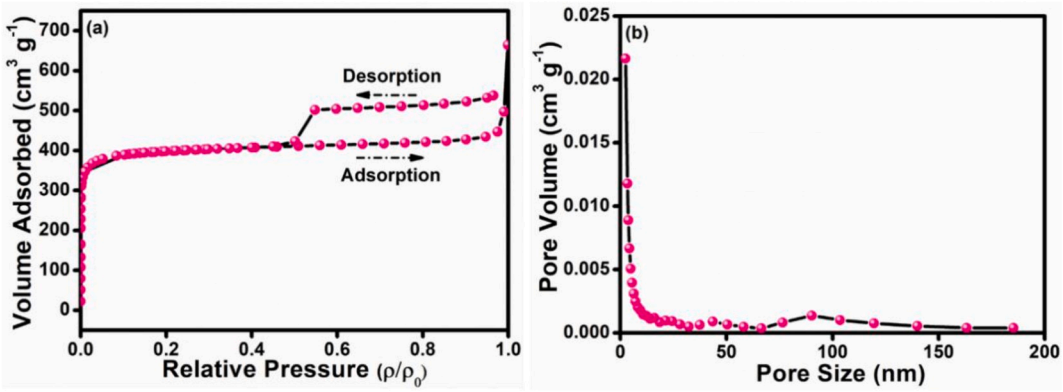

Fig. 7. a) Nitrogen adsorption/desorption isotherm and b) BJH pore size distributions of KAC-3 material.

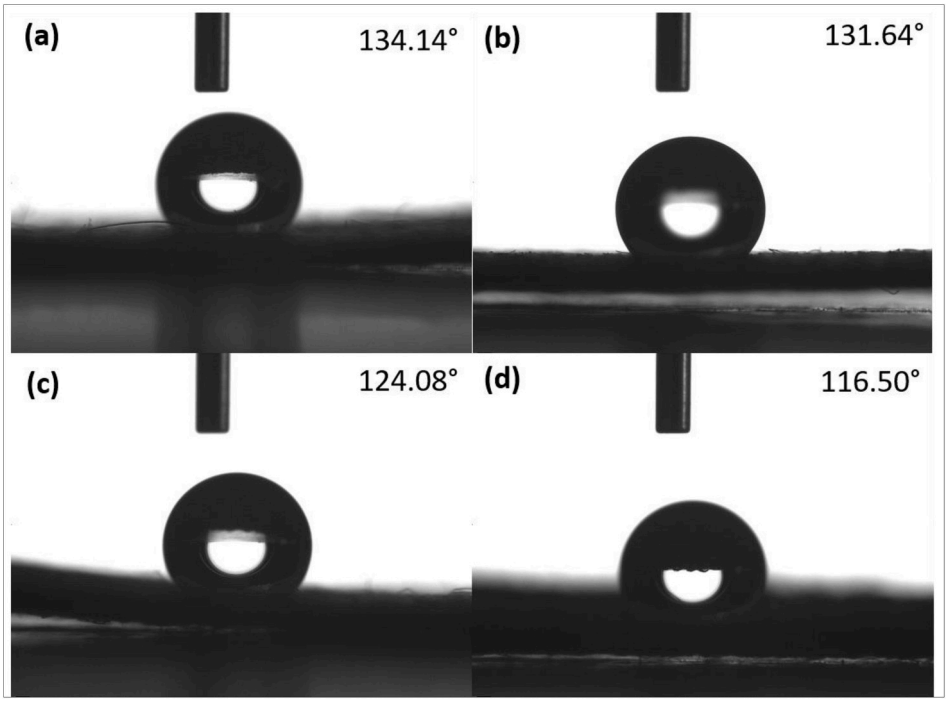

Fig. 8. The contact angle measurement of a) bare carbon cloth, b) KAC-1, c) KAC-2 and d) KAC-3 modified carbon cloth electrodes in 1 M H_2SO_4 electrolyte.

belongs to both type-I and type-IV isotherm, which indicates the presence of micropores, mesopores and little macropores distribution on the surface of KAC-3 material [2,6]. Also, the BET Specific surface area calculated for KAC-3 from N_2 adsorption/desorption isotherm (Fig. 7a) is about 1556 m^2 g^{-1}. The density of pores is maximum <5 nm, which belongs to the microporous network while ~10–30 nm belongs to the mesoporous network. The density of mesopores is maximum in KAC-3 material, and the calculated mean pore diameter is 2 nm, and total pore volume is 0.78 cm^3 g^{-1}, found from the BJH pore size distribution (Fig. 7b). The existence of mesoporosity is in good agreement with the FE-SEM (Fig. 5) and TEM (Fig. 6) analysis. In general, these mesoporous network is expected to serve as the reservoir for storing charge species and help in ion transportation during EDLC reaction, which enhances the overall electrochemical performance of the EDLC system [30].

The contact angle measurement was carried out on KAC-materials modified carbon cloth electrodes in 1 M H_2SO_4 shown in Fig. 8. All the electrodes exhibit a contact angle is greater than 100°, with a spherical droplet, denotes the hydrophobic nature of the surface. Jian Tan et al., have stated that pure carbon materials are hydrophobic, which prevents the electrolyte from getting into small pores, which limits the effective surface area of the electrode material [46]. Herein, as compared to the bare carbon cloth (Fig. 8a) the hydrophobicity of the KAC-materials modified carbon cloth electrodes decreases with increase in material porosity, in the order of KAC-3< KAC-2 < KAC-1, Fig. 8 (b–d). These results indicate that the wettability of KAC-3 modified carbon cloth is better than that of other electrodes with less hydrophilicity. Very recently, Ya Liu et al., have stated that the wettability of heteroatoms on the carbon surface can introduce more polar bonds and oxygenic groups, which is highly beneficial for enhancing the electrochemical performanceof supercapacitors [47]. Therefore, KAC-3 modified carbon cloth electrode is anticipated to be a promising candidate for enhancing the performance of EDLCs.

3.3. *Electrochemical properties (three-electrode system)*

For identifying the suitable electrode to fabricate the EDLC, the CV (Fig. 9) analysis is carried out for all the KAC-materials using a three electrodes system in 1 M H_2SO_4 electrolyte. Fig. 9a shows the comparative CV curve of the carbon cloth modified KAC- electrodes in 1 M H_2SO_4 at a scan rate of 10 mV s^{-1}. It exhibits the electrochemical

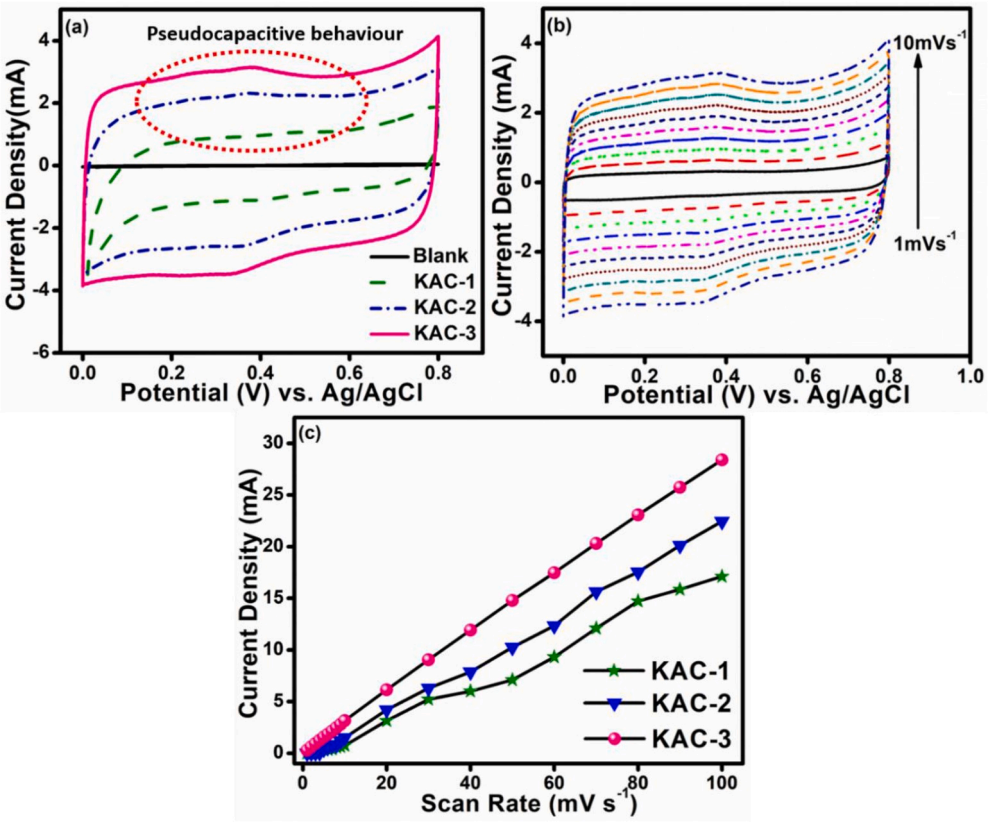

Fig. 9. a) CV profile of KAC electrodes at a fixed scan rate of 10 mV s^{-1}, b) CV of KAC-3 at different scan rate (1–10 mV s^{-1}) and c) Scan rate *vs.* current of KAC electrodes.

performances of both rectangular-shaped EDLC and pseudocapacitive behaviour (due to carboxylic functional group organization, as well as oxygen and nitrogen functionalities). The calculated specific capacitance from CV (Fig. 9a) at a scan rate of 10 mV s^{-1} for bare carbon cloth, KAC-1, KAC-2 and KAC-3 electrodes are 7.3, 212, 433 and 797 F g^{-1}, respectively. Overall, the KAC-3 electrode provides a higher specific capacitance than the rest of the electrodes. Fig. 9b shows the electrochemical performance of KAC-3 modified carbon cloth electrode at different scan rates (1–10 mV s^{-1}) in the same 1 M H_2SO_4 electrolyte. This means the reliability of the adsorption and desorption of the charged species are conserved, as it shows a symmetrical behaviour even at a higher scan rate. Also, the area under the CV (Fig. 9b) curve elevates with an increase in scan rate, which reveals that increase in scan rate facilitates high ion transportation through the electrolyte, which strongly impacts the double layer formation. Besides, Fig. 9c shows the discharge current obtained for all the KAC electrodes at various scan rates (1–100 mV s^{-1}). From the observation, it is clear that the discharge current increases with the increase in scan rate.

Fig. 10a shows the comparative GCD curve of all the KAC-electrodes in 1 M H_2SO_4 electrolyte measured at 2 mA cm^{-2} current density. The obtained specific capacitance (C_{SP}) from GCD for KAC-3 (312 F g^{-1}) electrode is high when compared to bare (1 F g^{-1}), KAC-1 (44 F g^{-1}), and KAC-2 (97 F g^{-1}) modified carbon cloth electrodes. Fig. 10b shows the GCD profile of KAC-3 electrode obtained at different current densities (1–6 mA cm^{-2}). Similarly, Fig. 10c shows the relationship between the calculated specific capacitance and current density of all the KAC electrodes. It can be seen that the specific capacitance of KAC- electrodes decrease gradually with respect to the increase in current. The attained specific capacitance of KAC-3 electrode is much higher than the reported biomass-derived carbon-based electrodes including, carbonated soft drink (Coca-Cola) (252 F g^{-1}) [48], loofah sponge (309 Fg^{-1}) [49], lotus seed shell (286 F g^{-1}) [50], baobab fruit shell (233 F g^{-1}) [51], Rapeseed dreg (170 F g^{-1}) [52]. Moreover, the organic functional group organization on the carbon surface provides large active sites for the charge to store during a redox reaction. KAC-3 electrode exhibited higher capacitance, due to its higher surface area, total pore volume, and organic surface functionalities organized on the surface which offers the large active site for ions to facilitate. The result indicates that the higher coulombic efficiency and capacitive performance of the KAC-3 electrode in 1 M H_2SO_4 is higher compared to other two electrodes.

The electrochemical impedance analysis was carried to understand the resistance exhibited by the KAC materials in a three-electrode system. Fig. 11a shows the Nyquist plot for KAC- electrodes measured in 1 M H_2SO_4 electrolyte using the three-electrode system. The Nyquist plot of KAC-materials, identified with similar behaviour, consisting of a semicircle at a mid-high frequency and a straight line at the low-frequency region. The obtained solution (R_s) and charge transfer (R_{ct}) resistances (Table 3) decreases in the order of KAC-3 < KAC-2 < KAC-1 electrodes. It infers that the electrochemical reactions can occur quickly in KAC-3 electrode. Fig. 11(b and c) shows the Bode plot of KAC electrodes, which reveals that, the impedance decreases with increase in frequency. The calculated specific capacitance (Fig. 11b) of KAC-3 electrode (282 F g^{-1}) is comparatively higher than the KAC-2 (164 F g^{-1}) and KAC-1 (98 F g^{-1}) electrodes, which is in concord with the CV and GCD results. Fig. 11c shows the frequency dependence of phase angle (θ), where θ increases in the order of KAC-3 (59°) < KAC-2 (55°) < KAC-1 (51°), modified CC electrodes, which infers the ideal capacitive nature of the electrodes, due to the role of organic functionalities and heteroatoms distribution on the surface carbon materials. Moreover, the relaxation time (τ) is calculated for all the KAC electrodes at a phase angle 45° (Fig. 11c), Where, τ attained for KAC-3 (118.8 s) is high compared to KAC-1 (65.2 s), KAC-2 (95.5 s), reveals the actual time taken by the electrodes during discharge phenomenon to deliver high energy output. Fig. 11d shows the relation between the real capacitance

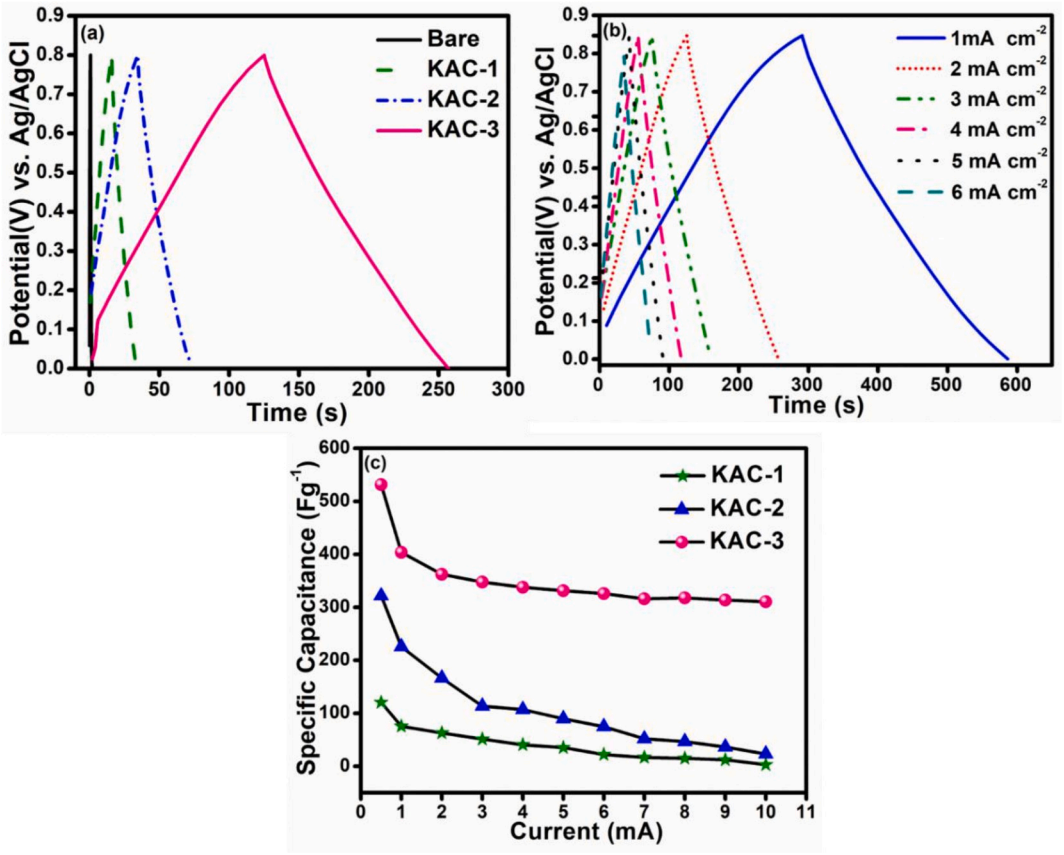

Fig. 10. a) GCD profile of KAC electrodes at 2 mA b) GCD of KAC-3 at different current (1–6 mA cm^{-2}), (c) current *vs* specific capacitance of KAC electrodes.

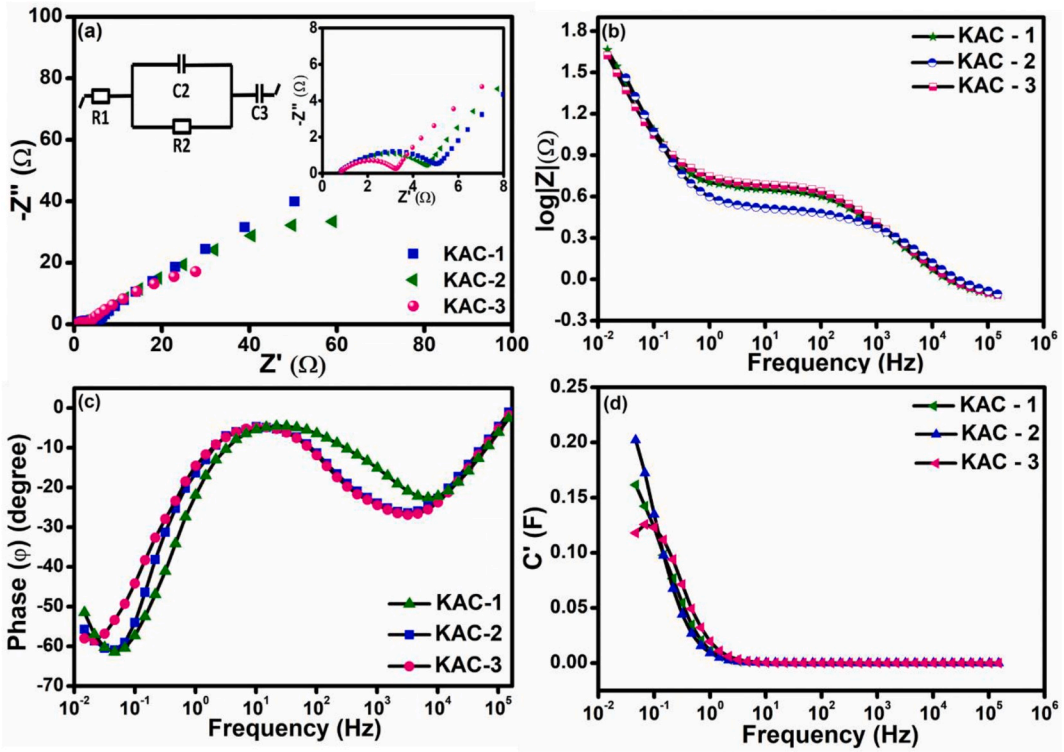

Fig. 11. a) Nyquist plot, b, c) Bode plot, and d) C' (F) vs. Frequency.

Table 3
Parameters calculated from electrochemical impedance spectroscopy.

Sample	Rs (Ω)	Rct (Ω)	Capacitance	Phase angle	C' (mF)
KAC-1	0.94	3.46	41 Fg^{-1}	−107.02	20
KAC-2	0.92	3.11	54 Fg^{-1}	−73.3	16
KAC-3	0.85	2.07	115 Fg^{-1}	−43.6	11.6

component (C') and the frequency. It can be seen that the specific capacitance is high in the low-frequency region for all the KAC electrodes. Amongst, the specific capacitance acquired for KAC-3 (20 mF g^{-1}) is high compared to KAC-2 (16 mF g^{-1}) and KAC-1 (11.6 mF g^{-1}) electrodes, which reveals the complete charged state of the electrode due to reasonable access to the electrolyte ions.

Overall, when compared to KAC-1 and KAC-2 electrodes, the electrochemical performance of KAC-3 in a three-electrode system is found to be superior in all aspects of electrochemical behaviour. It is because of large micropores (FE-SEM analysis) distributed on the carbon surface, which contributes low internal resistance for the ions to traverse in and out of the electrolytic medium. Moreover, the KAC-3 electrode having a large amount of pyrrolic nitrogen species than the other electrodes, which contributed the main charge-discharge reactions. Hence, KAC-3 modified carbon cloth electrode is considered to be a promising electrode for the fabrication of EDLC.

3.4. Electrochemical properties of the fabricated device (two-electrode system)

Based on the previous studies, the ELDC is fabricated using the optimized KAC-3 electrode and studied their electrochemical performances in both 1 M H_2SO_4 and 1 M H_2SO_4 + 0.05 M $VOSO_4$ electrolytes, where 0.05 M $VOSO_4$ is used as the redox additive to improve the electrochemical charge storage properties. Fig. 12a shows the corresponding CV curve of the devices measured at 2 mV s^{-1} scan rate. It can be seen that the typical rectangular shape is observed for the EDLC measured in 1 M H_2SO_4 electrolyte. On the other hand, quasi-rectangular behaviour with well-defined redox peaks is obtained in 1 M H_2SO_4 + 0.05 M $VOSO_4$ electrolyte, which reveals the redox reaction between the VO^{2+}/VO_2^+ species. The calculated specific capacitance of the device is 254 Fg^{-1} and 832 Fg^{-1} in 1 M H_2SO_4 and 1 M H_2SO_4 + 0.05 M $VOSO_4$ electrolytes, respectively. The attained specific capacitance from CV profile with $VOSO_4$ as redox additive electrolyte is superior compared to the recent works (Table 3), is due to the occurrence of redox reactions attributable to the presence of surface functionalities and redox mediator, which access fast ionic transport at the electrode-electrolyte interfaces. Fig. 12(b and c) shows the CV profile of the fabricated EDLC in 1 M H_2SO_4 in the absence and presence of 0.05 M $VOSO_4$ at different scan rates (5, 10, 20, 40, 60, 80 and 100 mVs^{-1}), respectively. Both the rectangular shape (in 1 M H_2SO_4) and quasi-rectangular shape (0.05 M $VOSO_4$ added 1 M H_2SO_4) is maintained well even after the higher scan rate (100 mV s^{-1}) in the CV profiles. Conspicuously, Fig. 12d shows the linearity of discharge current with respect to an increase in scan rate indicates the faster transportation of electrolytic ions into the bulk electrode. Therefore, the introduction of redox additive species into this electrolyte is further improved the electrochemical performance of the EDLC system.

Also, Fig. 13a shows the GCD response of the KAC-3 device in 1 M H_2SO_4 with the absence and presence of 0.05 M $VOSO_4$ electrolyte at a constant current of 5 mA. From the analysis, a simple isosceles triangle-shaped linear profile is attained in 1 M H_2SO_4, while in 0.05 M $VOSO_4$ added 1 M H_2SO_4, the GCD profile is quasi-isosceles during the discharge, due to the significant role played by the redox couples VO^{2+}/VO_2^+. As anticipated, higher discharge current was attained for 0.05 M $VOSO_4$ added 1 M H_2SO_4 based system, due to the redox reaction occurring between VO^{2+}/VO_2^+. In accordance, the specific capacitance of the EDLC is 92 Fg^{-1} and 133 Fg^{-1} at 5 mA in 1MH_2SO_4 and 1 M H_2SO_4

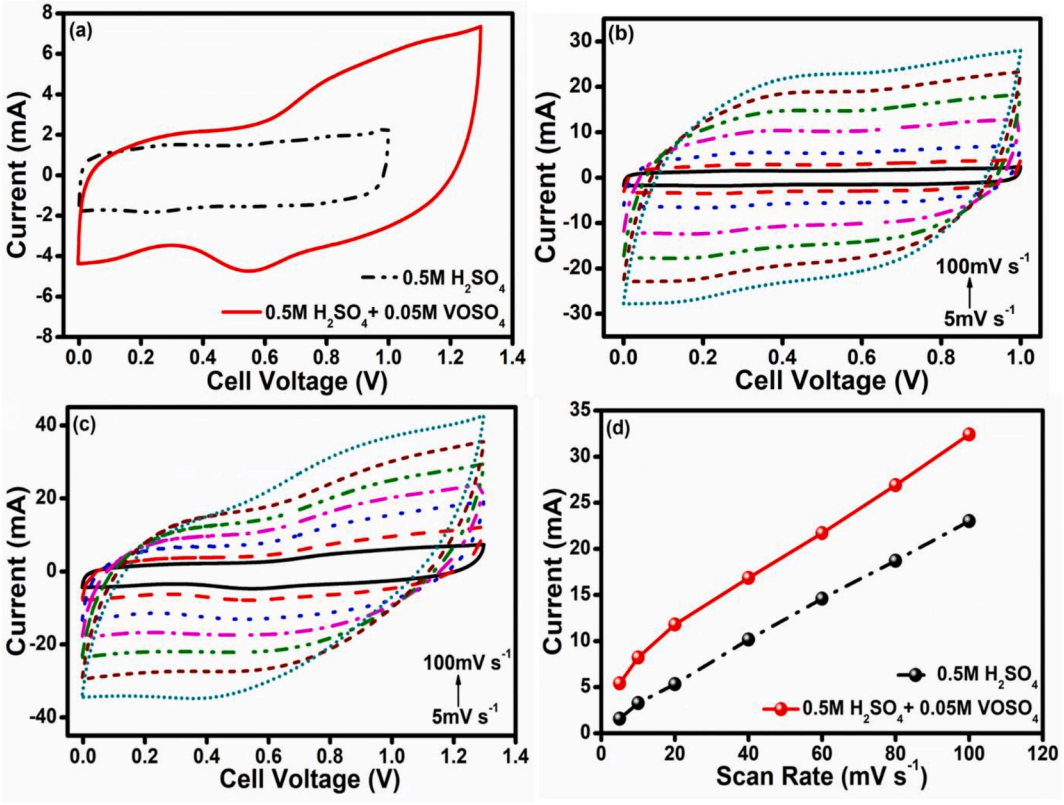

Fig. 12. a) CV profile of KAC-3 based EDLC at a scan rate of 2 mV s^{-1}, CV profile of KAC-3 based EDLC b) in H_2SO_4 and c) $VOSO_4$ added H_2SO_4 electrolyte at different scan rates (5–100 mV s^{-1}), d) scan rate vs. current of KAC -3 devices.

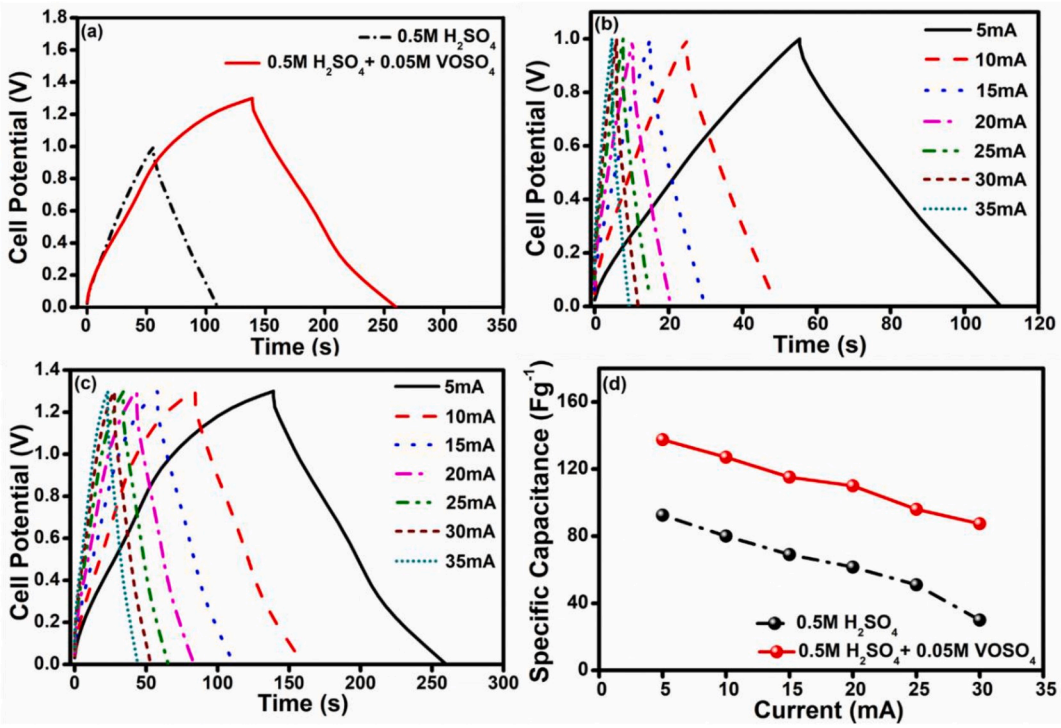

Fig. 13. a) GCD profile of KAC-3 based EDLC at a current of 5 mA, GCD profile of KAC-3 based EDLC b) in H_2SO_4 and c) $VOSO_4$ added H_2SO_4 electrolyte at different currents (5–35 mA), d) current vs. specific capacitance of KAC -3 devices.

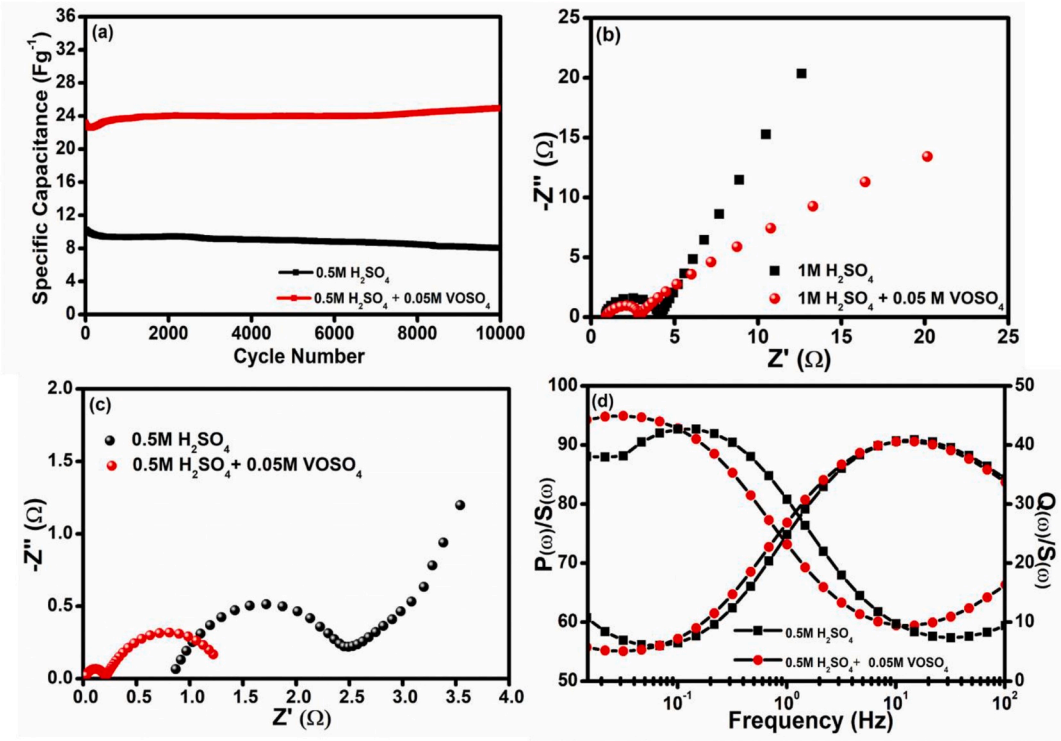

Fig. 14. a) Cycling stability of the KAC-3 device, EIS spectra of KAC-3 device measure b) before and c) after cycling, d) Frequency dependence of the fraction of the total reactive P(ω)/S(ω) and active Q(ω)/S(ω) power for the KAC-3 device.

+ 0.05 M $VOSO_4$, respectively.

Fig. 13(b and c) shows the GCD profile of the EDLC in 1 M H_2SO_4 and 1 M H_2SO_4 added 0.05 M $VOSO_4$ at different current (5–35 mA), respectively. It is seen from the CV profiles, both the rectangular shape (in 1 M H_2SO_4) and quasi-rectangular shape (0.05 M $VOSO_4$ added 1 M H_2SO_4) is maintained well even after the higher discharge current of 35 mA. Similarly, the linearity and quasi-isosceles triangle-shaped GCD profile are retained in 1 M $VOSO_4$ both in the absence and presence of 1 M H_2SO_4, respectively. This infers the superior rate capability of the EDLC during the charge/discharge process due to the combined efficacy

of 3D linked porous architecture and surface functionalities. Fig. 13d shows the calculated specific capacitance from the GCD curve of KAC-3 device at different currents. The obtained higher capacitance in the 0.05 M $VOSO_4$ added 1 M H_2SO_4 electrolyte is not only due to the electric double-layer capacitance but also because of the faradaic reaction of VO^{2+}/VO_2^+ at electrode/electrolyte interface. These results are ascribed with the peculiar properties of KAC-3 material and kinetics reaction between the redox couples VO^{2+}/VO_2^+ at electrode/electrolyte interface, where the possible mechanism occurs, VO^{2+} reacts with water molecules, to form VO_2^+, protons (H^+) and electrons (e^-). In detail, during the electrochemical performance, the redox pair VO^{2+}/VO_2^+ at the electrode/electrolyte interfaces is stimulated by the functional groups organized on the surface of KAC-3 electrode via oxygen transfer. More specifically, during charging, the VO^{2+} adsorbed on the KAC-3 electrode replaces the H^+ creates a strong bond where the oxygen species gets transferred to form VO_2^+ by releasing of H^+ and e^-. Therefore, VO_2^+ diffuses into the H_2SO_4 electrolyte via H^+ exchange. While, VO^{2+} forms transition state with C═O groups, and reacts with water and penetrates back into H_2SO_4 with the release of H^+ and e^- [53].

Fig. 14a shows the cycling stability of the fabricated EDLC device measured in both the electrolyte at the higher discharge current of 55 mA for 10,000 consecutive charge-discharge cycles. From the analysis, the stability in terms specific capacitance of the device in the $VOSO_4$ added 1 M H_2SO_4 electrolyte is higher than that in 1 M H_2SO_4. The possible reason for the enhancement in cycling stability is due to the complete occurrence of redox reactions and the removal of polar oxygen functionalities [54]. Fig. 14(b and c) shows the Nyquist plot of the fabricated EDLC in 1 M H_2SO_4, and 0.05 M $VOSO_4$ added 1 M H_2SO_4 over the frequency range (100 kHz −0.1 Hz) before and after 10,000 cycles. Especially, after cycling, the shape of the Nyquist plot for the redox additive added 1 M H_2SO_4 is observed with two semicircles. The semicircle at higher and lower frequency is due to the electrolyte resistance and diffusion resistance, respectively. Moreover, After cycling the diameter of semicircle is decreased, which is due to the activation of redox couples. Hence, the solution resistance (R_s) has changed from 0.90 Ω (before cycling) to 0.53 Ω (after cycling), reveals that cycling has an insignificant effect on the fabricated device. The lowering of resistance contributes faster ionic transportation through the electrolyte, and thus exhibits superior electrochemical performances.

Also, the charge transfer resistance dropped down from 7.6 Ω (before cycling) to 3.2 Ω (after cycling), which is due to the redox-additive electrolyte that delivers enhancement in ionic conductivity at the electrode-electrolyte interfaces [55,56]. Mainly, VO^{2+}/VO_2^+ exhibits mixed control due to the transfer of charge species at the electrolyte/electrode interface and participate in easy diffusion process in the pores of activated carbon material, respectively. Further, Fig. 14d shows the frequency dependence of the fraction of the total reactive P(ω)/S(ω) and active Q(ω)/S(ω) power for the EDLC device in H_2SO_4 and H_2SO_4 + $VOSO_4$ electrolytes. In general, EDLCs acts as a capacitor at low and as a resistor at high-frequency regions. Hence, the output power has both active P(ω)/S(ω) and reactive Q(ω)/S(ω) components, which is evaluated using the following equation,

$$\frac{P(\omega)}{S(\omega)} = \frac{\omega C''(\omega)|\Delta V_{rms}|^2}{-\omega C(\omega)|\Delta V_{rms}|^2} \quad (12)$$

$$\frac{Q(\omega)}{S(\omega)} = \frac{-\omega C'(\omega)|\Delta V_{rms}|^2}{-\omega C(\omega)|\Delta V_{rms}|^2} \quad (13)$$

Where, $|\Delta V_{rms}|^2 = \Delta V_{max}/\sqrt{2}$, with ΔV_{max} as the maximum amplitude of the a.c signal.

Both the devices exhibited ~100% reactive power Q(ω)/S(ω) in the high-frequency region while the active power P(ω)/S(ω) gets decreased towards the high-frequency region. It infers, how rapidly the active power gets dissipated into the system at high frequency due to the resistive nature of the system. The cut-off behaviour found in the mid-frequency region describes the transition from capacitive to a resistive behaviour of the electrode in the EDLC system. Also, the relaxation time (τ), calculated from the plot (Fig. 14d), corresponding to the cut-off frequency, which is found to be higher in 0.5 M H_2SO_4 + 0.05 M $VOSO_4$ (11.75 s) electrolytes than in 0.5 M H_2SO_4 (7.36 s) electrolyte. Therefore, from the observation, it is clear that KAC-3 device has higher power delivery output with low resistive behaviour and has high capacitive nature.

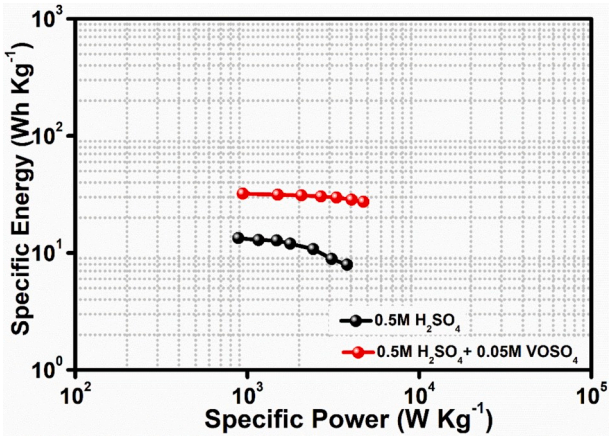

Fig. 15. Ragone plot of KAC-3 device.

Fig. 15 shows the Ragone plot of the device, which correlates the relationship between the specific energy and power of the device. The calculated specific energy of the device in 1 M H_2SO_4 is 13 Wh kg^{-1} at 885 kW kg^{-1}. On the other hand, almost 2.5 times the higher specific energy of 32 Wh kg^{-1} at 941 kW kg^{-1} is observed in 0.05 M $VOSO_4$ added 1 M H_2SO_4 electrolyte. For comparison, Table 4 provides the specific energy and specific power of the reported kinds of literature. Among these, the specific energy obtained by KAC-3 based EDLC is twice than that of Corn silks (17.8 Wh kg^{-1}) [15], watermelon rind (12.9 Wh kg^{-1}) [16], Konjaku Flour (9.2 Wh kg^{-1}) [17], charcoal (1.85 Wh kg^{-1}) [18], Activated carbon (17.81 Wh kg^{-1}) [19], and Glucose (14.53 Wh kg^{-1}) [21]. The reason is that the KAC-3 based EDLC has a higher surface area, significant nitrogen content, 3D porous architecture compared to the reported works, which acts as a reservoir to facilitate ion transportation and improvise the overall electrochemical performance of the device. Especially, the redox additive electrolyte with VO^{2+}/VO_2^+ redox pair improvises the faradaic capacitance and thus improvises the electrochemical properties of the device. Therefore, the redox-mediated device with 3D mesoporous carbon electrode exhibiting high specific energy and power is a promising factor for its potential usage in fast-charge EDLC application.

4. Conclusion

Natural sea-sponge like 3D mesoporous carbon was prepared from *Artocarpus heterophyllus* seeds derived starch through hydrothermal treatment followed by KOH activation. The amorphous nature and high degree of graphitization have been confirmed through XRD and Raman analysis. The presence of organic functional groups due to tartaric acid catalysation during hydrothermal treatment is revealed through FTIR analysis. The porous morphology of the activated carbon surface is understood through FE-SEM and TEM analysis. More specifically, the EDLC fabricated using activated carbo electrode, and 1 M H_2SO_4 added with $VOSO_4$ electrolyte showed a maximum specific capacitance of 133 Fg^{-1} at 5 mA which is greater than that of specific capacitance delivered by 1 M H_2SO_4 (92 Fg^{-1}). Successively, the energy density is also increased from 13 to 32 W h kg^{-1}, respectively. From the overall electrochemical measurement, it is clear that the redox additive with VO^{2+}/VO_2^+ improvises the electrochemical properties of AC carbon-based EDLC.

Table 4
Comparison of electrochemical parameters with reported work.

Precursor	Support electrolyte	Redox mediator	Specific capacitance	Specific Energy (Wh kg^{-1})	Specific Power (W kg^{-1})	Columbic efficiency (%) and cycles	Ref
Poplar catkins	KOH	PPD	254 F g^{-1} at 10 mA	–	–	77.4% and 500 cycles	[14]
Corn silks	H_2SO_4	alizarin red and bromoamine acid	169.2 F g^{-1} at 8 mA	17.8	360	1000 cycles	[15]
Watermelon rind	KOH	PPD	260 Fg^{-1} at 1 mA	12.9	250	93.8% with 5000 cycles	[16]
Konjaku Flour	KOH	PPD	40.5 Fg^{-1} at 5 mA	9.2	250	93.7% with 5000 cycles	[17]
Charcoal	H_2SO_4	Hydroquinone and PPD	116.2 Fg^{-1} at 2 Ag^{-1}	1.85	150	90% and 2000 cycles	[18]
Activated carbon	KOH	$K_3Fe(CN)_6$	229.17 Fg^{-1} at 1 Ag^{-1}	17.81	–	–	[19]
Glucose	H_2SO_4	KI	654 Fg^{-1} at 2 Ag^{-1}	14.53	402	92% and 4000 cycles	[21]
AHS	H_2SO_4	$VOSO_4$	832.5 Fg^{-1} at 2 mVs^{-1} 133 Fg^{-1} at 5 mA	32.4	936.5	97.6% and 10,000 cycles	Present work

Declaration of competing interest

The authors declare that they have no known competing financial interests or personal relationships that could have appeared to influence the work reported in this paper.

CRediT authorship contribution statement

Palanisamy Rupa Kasturi: Conceptualization, Investigation, Writing - original draft. **Ramasamy Harivignesh:** Resources. **Yun Sung Lee:** Resources. **Ramakrishnan Kalai Selvan:** Conceptualization, Supervision.

Acknowledgement

Prof. Yun Sung Lee acknowledges the Ministry of Science, ICT and Future Planning of South Korea for providing a National Research Foundation of Korea (NRF) grant (No.2019R1A4A2001527).

References

[1] D. Liu, L. Tao, D. Yan, Y. Zou, S. Wang, Recent advances on non-precious metal porous carbon-based electrocatalysts for oxygen reduction reaction, ChemElectroChem 5 (2018) 1775–1785.
[2] L. Wang, X. Hu, Recent advances in porous carbon materials for electrochemical energy storage, Chem. Asian J. 13 (12) (2018) 1518–1529.
[3] A.A.C. Riojas, A. Wong, G.A. Planes, M.D. Sotomayor, A. La Rosa-Toro, A. M. Baena-Moncada, Development of a new electrochemical sensor based on silver sulfide nanoparticles and hierarchical porous carbon modified carbon paste electrode for determination of cyanide in river water samples, Sensor. Actuator. B Chem. 287 (2019) 544–550.
[4] C. Hu, Y. Lin, J.W. Connell, H.M. Cheng, Y. Gogotsi, M.M. Titirici, L. Dai, Carbon-based metal-free catalysts for energy storage and environmental remediation, Adv. Mater. 31 (2019) 1806128.
[5] R.J. White, Porous Carbon Materials from Sustainable Precursors, R. Soc. Chem. 1 (2015) 1–354.
[6] K. Ishizaki, S. Komarneni, M. Nanko, Porous Materials: Process Technology and Applications, vol. 1, Springer Science & business media, 2013, pp. 1–240.
[7] B.E. Conway, Electrochemical Supercapacitors: Scientific Fundamentals and Technological Applications, vol. 1, Springer Science & Business Media, 2013, ISBN 978-0-306-45736-4, pp. 1–698.
[8] T. Sato, Science, Technology and Advanced Application of Supercapacitors 1, 2019, pp. 1–19.
[9] N. Rey-Raap, M. Enterría, J.I.c. Martins, M.F.R. Pereira, J.L.s. Figueiredo, Influence of multiwalled carbon nanotubes as additives in biomass-derived carbons for supercapacitor applications, ACS Appl. Mater. Interfaces 11 (2019) 6066–6077.
[10] A. Mishra, G. Bera, P. Mal, G. Padmaja, P. Sen, P. Das, B. Chakraborty, G. Turpu, Comparative electrochemical analysis of rGO-FeVO4 nanocomposite and $FeVO_4$ for supercapacitor application, Appl. Surf. Sci. 488 (2019) 221–227.
[11] T.F. Zhang, Q.X. Xia, Z. Wan, J.M. Yun, Q.M. Wang, K.H. Kim, Highly porous carbon nanofoams synthesized from gas-phase plasma for symmetric supercapacitors, Chem. Eng. J. 360 (2019) 1310–1319.
[12] Y. Nan, B. Li, X. Song, N. Sano, Optimization of pore-opening condition in single-walled carbon nanohorns to achieve high capacity in double layer capacitor at high charge-discharge rate: critical effect of their hierarchical pore structures, Carbon 142 (2019) 150–155.
[13] S. Joseph, D.M. Kempaiah, M.R. Benzigar, H. Ilbeygi, G. Singh, S.N. Talapaneni, D.-H. Park, A. Vinu, Highly ordered mesoporous carbons with high specific surface area from carbonated soft drink for supercapacitor application, Microporous Mesoporous Mater. 280 (2019) 337–346.
[14] L. Liu, R. Feng, Y. Pan, X. Zheng, L. Bai, Nanoporous carbons derived from poplar catkins for high performance supercapacitors with a redox active electrolyte of p-phenylenediamine, J. Alloys Compd. 748 (2018) 473–480.
[15] K. Sun, Z. Zhang, H. Peng, G. Zhao, G. Ma, Z. Lei, Hybrid symmetric supercapacitor assembled by renewable corn silks based porous carbon and redox-active electrolytes, Mater. Chem. Phys. 218 (2018) 229–238.
[16] X.-Q. Lin, N. Yang, Q.-F. Lü, R. Liu, Self-nitrogen-Doped porous bio-carbon from watermelon rind: a high-performance supercapacitor electrode and its improved electrochemical performance using redox additive electrolyte, Energy Technol. 7 (2019), 1800628.
[17] X.-Q. Lin, Q.-F. Lü, Q. Li, M. Wu, R. Liu, Fabrication of low-cost and eco-friendly porous bio-carbon using Konjaku Flour as the raw material for high-performance supercapacitor application, ACS Omega 3 (2018) 13283–13289.
[18] Y.-C. Chen, L.-Y. Lin, Investigating the redox behaviour of activated carbon supercapacitors with hydroquinone and p-phenylenediamine dual redox additives in the electrolyte, J. Colloid Interface Sci. 537 (2019) 295–305.
[19] E. Elaiyappillai, R. Srinivasan, Y. Johnbosco, P. Devakumar, K. Murugesan, K. Kesavan, P.M. Johnson, Low cost activated carbon derived from Cucumis melo fruit peel for electrochemical supercapacitor application, Appl. Surf. Sci. 486 (2019) 527–538.
[20] Y. Ma, M. Chen, X. Zheng, D. Yu, X. Dong, Synergetic effect of swelling and chemical blowing to develop peach gum derived nitrogen-doped porous carbon nanosheets for symmetric supercapacitors, J. Taiwan Inst. Chem. Eng. 101 (2019) 24–30.
[21] H. Jia, S. Wang, J. Sun, K. Yin, X. Xie, L. Sun, Nitrogen-doped microporous carbon derived from a biomass waste-metasequoia cone for electrochemical capacitors, J. Alloys Compd. 794 (2019) 163–170.
[22] P.R. Kasturi, H. Ramasamy, D. Meyrick, Y.S. Lee, R.K. Selvan, Preparation of starch-based porous carbon electrode and biopolymer electrolyte for all solid-state electric double layer capacitor, J. Colloid Interface Sci. 554 (2019) 142–156.
[23] P.R. Kasturi, A. Arunchander, D. Kalpana, R.K. Selvan, Bio-derived carbon as an efficient supporting electrocatalyst for the oxygen reduction reaction, J. Phys. Chem. Solid. 124 (2019) 305–311.
[24] R.K. Selvan, Y.S. Lee, Pt decorated Artocarpus heterophyllus seed derived carbon as an anode catalyst for DMFC application, RSC Adv. 6 (2016) 62680–62694.
[25] S. Senthilkumar, R.K. Selvan, Y. Lee, J. Melo, Electric double layer capacitor and its improved specific capacitance using redox additive electrolyte, J. Mater. Chem. 1 (2013) 1086–1095.
[26] S. Roldán, C. Blanco, M. Granda, R. Menéndez, R. Santamaría, Towards a further generation of high-energy carbon-based capacitors by using redox-active electrolytes, Angew. Chem. Int. Ed. 50 (2011) 1699–1701.
[27] E. Frackowiak, M. Meller, J. Menzel, D. Gastol, K. Fic, Redox-active electrolyte for supercapacitor application, Faraday Discuss 172 (2014) 179–198.
[28] S. Senthilkumar, R.K. Selvan, N. Ponpandian, J. Melo, Y. Lee, Improved performance of electric double layer capacitor using redox additive (VO^{2+}/VO^{2+}) aqueous electrolyte, J. Mater. Chem. 1 (2013) 7913–7919.
[29] M.T. Reza, E. Rottler, L. Herklotz, B. Wirth, Hydrothermal carbonization (HTC) of wheat straw: influence of feedwater pH prepared by acetic acid and potassium hydroxide, Bioresour. Technol. 182 (2015) 336–344.
[30] J. Liang, Y. Liu, J. Zhang, Effect of solution pH on the carbon microsphere synthesized by hydrothermal carbonization, Procedia Environ. Sci. 11 (2011) 1322–1327.
[31] H. Mao, X. Chen, R. Huang, M. Chen, R. Yang, P. Lan, M. Zhou, F. Zhang, Y. Yang, X. Zhou, Fast preparation of carbon spheres from enzymatic hydrolysis lignin: effects of hydrothermal carbonization conditions, Sci. Rep. 8 (2018) 9501.
[32] J. Gawronski and K. Gawronska, ISBN: 978-0-471-24451-6, John Wiley & Sons, 1, (1999) 616.

[33] M. Pal, R. Rakshit, K. Mandal, Surface modification of $MnFe_2O_4$ nanoparticles to impart intrinsic multiple fluorescence and novel photocatalytic properties, ACS Appl. Mater. Interfaces 6 (2014) 4903–4910.
[34] M.A. Prathap, B. Kaur, R. Srivastava, Hydrothermal synthesis of CuO micro-/nanostructures and their applications in the oxidative degradation of methylene blue and non-enzymatic sensing of glucose/H_2O_2, J. Colloid Interface Sci. 370 (2012) 144–154.
[35] E. Golestani, M. Javanbakht, H. Ghafarian-Zahmatkesh, H. Beydaghi, M. Ghaemi, Tartaric acid assisted carbonization of LiFePO4 synthesized through in situ hydrothermal process in aqueous glycerol solution, Electrochim. Acta 259 (2018) 903–915.
[36] T. Liu, Y. Li, H. Zhang, M. Wang, X. Fei, S. Duo, Y. Chen, J. Pan, W. Wang, Tartaric acid assisted hydrothermal synthesis of different flower-like ZnO hierarchical architectures with tunable optical and oxygen vacancy-induced photocatalytic properties, Appl. Surf. Sci. 357 (2015) 516–529.
[37] S.K. Hoekman, A. Broch, C. Robbins, Hydrothermal carbonization (HTC) of lignocellulosic biomass, Energy Fuel. 25 (2011) 1802–1810.
[38] B. Manoj, A. Kunjomana, Study of stacking structure of amorphous carbon by X-ray diffraction technique, Int. J. Electrochem. Sci 7 (2012) 3127–3134.
[39] N. Papaioannou, A. Marinovic, N. Yoshizawa, A.E. Goode, M. Fay, A. Khlobystov, M.-M. Titirici, A. Sapelkin, Structure and solvents effects on the optical properties of sugar-derived carbon nanodots, Sci. Rep. 8 (2018) 6559.
[40] W. Yu, H. Wang, S. Liu, N. Mao, X. Liu, J. Shi, W. Liu, S. Chen, X. Wang, N, O-co-doped hierarchical porous carbons derived from algae for high-capacity supercapacitors and battery anodes, J. Mater. Chem. 4 (2016) 5973–5983.
[41] J. Zhu, S. Dong, Y. Xu, H. Guo, X. Lu, X. Zhang, Oxygen-enriched crumpled graphene-based symmetric supercapacitor with high gravimetric and volumetric performances, J. Electroanal. Chem. 833 (2019) 119–125.
[42] S.W. Han, J. Bang, S.H. Ko, R. Ryoo, Variation of nitrogen species in zeolite-templated carbon by low-temperature carbonization of pyrrole and the effect on oxygen reduction activity, J. Mater. Chem. 7 (2019) 8353–8360.
[43] D.I. Abouelamaiem, G. He, I. Parkin, T.P. Neville, A.B. Jorge, S. Ji, R. Wang, M.-M. Titirici, P.R. Shearing, D.J. Brett, Synergistic relationship between the three-dimensional nanostructure and electrochemical performance in biocarbon supercapacitor electrode materials, Sustain. Energy Fuels 2 (2018) 772–785.
[44] W. Sun, S.M. Lipka, C. Swartz, D. Williams, F. Yang, Hemp-derived activated carbons for supercapacitors, Carbon 103 (2016) 181–192.
[45] N. Guo, M. Li, X. Sun, F. Wang, R. Yang, Enzymatic hydrolysis lignin derived hierarchical porous carbon for supercapacitors in ionic liquids with high power and energy densities, Green Chem. 19 (2017) 2595–2602.
[46] J. Tan, Y. Han, L. He, Y. Dong, X. Xu, D. Liu, H. Yan, Q. Yu, C. Huang, L. Mai, In situ nitrogen-doped mesoporous carbon nanofibers as flexible freestanding electrodes for high-performance supercapacitors, J. Mater. Chem. 5 (2017) 23620–23627.
[47] Y. Liu, X. Zhao, C. Wang, L. Zhang, M. Li, Y. Pan, Y. Fu, J. Liu, H. Lu, Egg albumen templated graphene foams for high-performance supercapacitor electrodes and electrochemical sensors, J. Mater. Chem. 6 (2018) 18267–18275.
[48] S. Joseph, D.M. Kempaiah, M.R. Benzigar, H. Ilbeygi, G. Singh, S.N. Talapaneni, D.-H. Park, A. Vinu, Highly ordered mesoporous carbons with high specific surface area from carbonated soft drink for supercapacitor application, Microporous Mesoporous Mater. 280 (2019) 337–346.
[49] X.-L. Su, J.-R. Chen, G.-P. Zheng, J.-H. Yang, X.-X. Guan, P. Liu, X.-C. Zheng, Three-dimensional porous activated carbon derived from loofah sponge biomass for supercapacitor applications, Appl. Surf. Sci. 436 (2018) 327–336.
[50] L. Hu, Q. Zhu, Q. Wu, D. Li, Z. An, B. Xu, Natural biomass-derived hierarchical porous carbon synthesized by an in situ hard template coupled with NaOH activation for ultrahigh rate supercapacitors, ACS Sustain. Chem. Eng. 6 (2018) 13949–13959.
[51] A.A. Mohammed, C. Chen, Z. Zhu, Low-cost, high-performance supercapacitor based on activated carbon electrode materials derived from baobab fruit shells, J. Colloid Interface Sci. 538 (2019) 308–319.
[52] X. Kang, H. Zhu, C. Wang, K. Sun, J. Yin, Biomass derived hierarchically porous and heteroatom-doped carbons for supercapacitors, J. Colloid Interface Sci. 509 (2018) 369–383.
[53] Y. Jin, Y. Meng, W. Fan, H. Lu, T. Liu, S. Wu, Free-standing Macro-Porous Nitrogen Doped Graphene Film for High Energy Density Supercapacitor, Electrochimica Acta, 2019.
[54] M. Zhang, G. Wang, L. Lu, T. Wang, H. Xu, C. Yu, H. Li, W. Tian, Improving the electrochemical performances of active carbon-based supercapacitors through the combination of introducing functional groups and using redox additive electrolyte, J. Saudi Chem. Soc. 22 (2018) 908–918.
[55] Y. Li, Z. Wang, L. Li, S. Peng, L. Zhang, M. Srinivasan, S. Ramakrishna, Preparation of nitrogen-and phosphorous co-doped carbon microspheres and their superior performance as anode in sodium-ion batteries, Carbon 99 (2016) 556–563.
[56] D. Jain, J. Kanungo, S. Tripathi, Enhanced performance of ultracapacitors using redox additive-based electrolytes, Appl. Phys. A 124 (2018) 124–397.